MATERIALS CHEMISTRY FRONTIERS

CHINESE CHEMICAL SOCIETY | ROYAL SOCIETY OF CHEMISTRY

RESEARCH ARTICLE

View Article Online
View Journal | View Issue

Check for updates

Cite this: Mater. Chem. Front., 2022, 6, 1091

In situ reconstruction of vegetable sponge-like Bi_2O_3 for efficient CO_2 electroreduction to formate†

Yingli Shi, Chun Fang Wen, Xuefeng Wu, Jia Yue Zhao, Fangxin Mao,* Peng Fei Liu and Hua Gui Yang*

Received 26th November 2021, Accepted 3rd March 2022

DOI: 10.1039/d1qm01557e

rsc.li/frontiers-materials

The electrochemical reduction reaction of CO_2 provides a renewable method to close the carbon cycle and alleviate the global energy issue. Bi-based electrocatalysts present huge prospects for catalyzing formate-selective CO_2 reduction. Herein, we fabricated a porous vegetable sponge-like bismuth oxide (VS-Bi_2O_3) for the selective electroreduction of CO_2 to formate, which underwent *in situ* reconstruction to form 2D nanosheets containing metallic Bi and $Bi_2O_2CO_3$. We propose that the unique porous morphology and low crystallinity of VS-Bi_2O_3 are beneficial for the *in situ* generation of $Bi_2O_2CO_3$, which might play a significant role in enhancing the CO_2 electrocatalysis performance. The catalyst delivers a 93.7% faradaic efficiency of formate at 400 mA cm^{-2} and shows stability for over 18 h at 100 mA cm^{-2}.

Introduction

The electrochemical CO_2 reduction reaction (CO_2RR) using renewable electricity sources is considered to be an ideal strategy for storing energy and relieving the global environment crisis caused by carbon emissions.[1–3] Through an electrocatalytic reaction, CO_2 could be converted into valuable chemicals and fuels such as formic acid, CO, methanol, ethanol, ethylene, and acetate.[4,5] Formic acid or formate, with a high energy density and versatile chemical features, can be applied in plenty of areas including pharmaceuticals, the leather industry, hydrogen storage, fuel cells, and metallurgy.[6,7] Its critical potential has been presented in industrial applications for reducing CO_2 to formate *via* electrocatalysis.[8,9] However, some obstacles, such as the sluggish reaction kinetics and high electricity consumption, need to be overcome before large-scale application. CO_2 is a linear molecule with the highest oxidation state, which means that it has a high thermodynamic stability (*i.e.*, 806 kJ mol^{-1} energy is needed to break the C=O bond).[4,10–14] A large reorganization energy in the first electron transfer step to form $CO_2^{\bullet-}$ from CO_2, −1.90 V *versus* the standard hydrogen electrode, imposes a high overpotential and a slow reaction rate.[15] Furthermore, the hydrogen evolution reaction (HER) competes with the desired CO_2RR, leading to a selectivity loss for the generation of formate.[3,11] Therefore, developing efficient electrocatalysts with low overpotentials and high selectivity becomes a key challenge for exclusively reducing CO_2 to formate.

Bismuth-based (Bi-based) materials, as efficient electrocatalysts, have aroused great interest in producing formic acid or formate from CO_2, due to their low cost, low toxicity and environmentally benign traits.[16–18] Due to the low carbon monoxide adsorption energy and strong stabilization of intermediates, Bi-based materials are thermodynamically favorable for yielding formate instead of competitive CO or H_2.[19,20] To implement the reaction, a high overpotential of over 300 mV must generally be applied along with a low current density (usually less than 100 mA cm^{-2}, especially in H cell system).[21,22] Structural engineering methods, such as morphology, component and defect engineering, have been reported to promote the catalytic activities of catalytic materials.[23,24] Earlier studies regarding Bi-based catalysts with different morphologies, including dendrites, nanowires, nanoflakes, bismuthene nanosheets as well as nanoparticles, have been reported to deliver a high formate selectivity of over 90%.[7,25] However, once they interact with the surrounding reactants or products under the reduction conditions, most of the catalysts are inclined to undergo structural self-reconstruction, which can change their morphology and structure, which thus further alters the activity and selectivity of the catalysts.[22,26] For instance, Yao *et al.* proposed that the $KHCO_3$ electrolyte could moderate the dissociation and conversion of the

Key Laboratory for Ultrafine Materials of Ministry of Education, Shanghai Engineering Research Center of Hierarchical Nanomaterials, School of Materials Science and Engineering, East China University of Science and Technology, 130 Meilong Road, Shanghai 200237, China. E-mail: hgyang@ecust.edu.cn, fxmao@ecust.edu.cn

† Electronic supplementary information (ESI) available. See DOI: 10.1039/d1qm01557e

Bi-based metal–organic framework (Bi-MOF) into $Bi_2O_2CO_3$, and the applied cathodic potential further helped to reduce the $Bi_2O_2CO_3$ to metallic Bi, of which the unsaturated surface Bi atoms served as active sites.[22] The work of Ma *et al.* reported bismuthene (Bi-ene) nanosheets derived from monoclinic scheelite $BiVO_4$ under working conditions, which significantly enhanced the CO_2 reduction performance.[27] We anticipate that designing new precatalysts with specific structures will play a significant role in developing highly efficient Bi-based catalysts.

Bi_2O_3, which has both high physical and chemical stability, is convenient for synthesis reactions without being much affected by the surrounding environment. This can help to rule out unnecessary influences and focus on the research priorities. Besides, Bi_2O_3 possesses CO_2RR advantages like other Bi-based materials. For example, the Bi–O structure of Bi_2O_3 has been reported to be conducive to CO_2RR *via* enhancing the CO_2 adsorption capacity and improving the stability of the $CO_2^{\bullet-}$ intermediate.[28,29] Many Bi-based catalysts with the Bi–O structure, such as Bi_2O_3 nanosheet/nitrogen-doped graphene quantum dots (Bi_2O_3-NGQDs),[30] β-Bi_2O_3 fractals[31] and Bi_2O_3 nanosheets grown on a conductive multi-channel carbon matrix (Bi_2O_3NS@MCCM),[32] exhibit a high CO_2RR performance. Our aim is to prepare a highly active Bi_2O_3 material and study its *in situ* reconstruction process in electrolytic CO_2 reduction.

Herein, a porous vegetable sponge-like bismuth oxide (VS-Bi_2O_3) was synthesized using a microwave ultrasonic synthesis method and exhibited an excellent performance for catalyzing CO_2 to formate with a faradaic efficiency (FE) of around 93% under a potential ranging from −0.53 to −1.29 V (*versus* the reversible hydrogen electrode (RHE)), where all potentials are referenced to RHE unless mentioned otherwise) and a current density up to 400 mA cm^{-2} in the flow cell system. *In situ* reconstruction of VS-Bi_2O_3 took place under CO_2RR conditions, with a fine nanosheet structure containing metallic Bi and $Bi_2O_2CO_3$ formed. The porous structure of VS-Bi_2O_3 might be favorable for reconstruction during the CO_2RR, and the generated $Bi_2O_2CO_3$ could maintain the superior catalytic performance of formate generation, with scarce attenuation occurring under a current density of 100 mA cm^{-2} over 18 hours.

Experimental section

Synthesis of materials

The VS-Bi_2O_3 was fabricated using a featured microwave ultrasonic synthesis method based on a previous report with modifications.[33] Firstly, 489.8 mg $Bi(NO_3)_3 \cdot 5H_2O$ and 505.0 mg dicyandiamide were ultrasonically dissolved in 50 mL ethylene glycol (EG) in sequence to form a clear solution using a special three-neck flask. Then the flask was assembled with the corresponding condensation glassware using a microwave/ultrasonic/UV combined catalytic synthesizer (XH-300UL-2+, Beijing Xianghu Science and Technology Development Co., Ltd). A constant-temperature heating mode was chosen to synthesize the VS-Bi_2O_3 sample. Typically, the microwave heating power was limited to the maximum of 300 W and the assisting ultrasonication was applied using a constant power of 500 W. The temperature was increased to 150 °C within 10 min and held there for another 10 min by the automatic program. The obtained white precipitate was then centrifugated and washed thoroughly using deionized water as well as ethanol in sequence. The white VS-Bi_2O_3 was obtained after drying at 60 °C for 12 h using a vacuum oven.

The produced VS-Bi_2O_3 was then calcined using a muffle furnace to fabricate the contrast bulk Bi_2O_3 (B-Bi_2O_3). The temperature was set as 500 °C and the furnace was supposed to reach that temperature in 100 minutes after which it remained at the same temperature for 1 h.

Characterization

X-Ray diffraction (XRD, D/max2550V) was carried out in order to interpret the crystal structure of the products. Scanning electron microscopy (SEM; Hitachi S4800) and transmission electron microscopy (TEM) were employed for the morphology change. Scanning transmission electron microscopy (STEM) and TEM characterization were performed using a Thermo Fisher Talos F200X instrument. Energy dispersive X-ray spectroscopy (EDS) was carried out using 4 in-column Super-X detectors. X-ray photoelectron spectroscopy (XPS; Thermo Escalab 250Xi) was carried out using an Al Kα X-ray beam (1486.6 eV) and was used to obtain more detailed information on the chemical compositions. In the meantime, the C 1s peak centered at 284.8 eV was set as the reference for calibration of all of the binding energies. Raman analysis was performed using a Leica DMLM microscope (Renishaw). The excitation wavelength and laser power were set as 532 nm and 3 mW, respectively.

Electrochemical measurements

The experiments were carried out using a home-made flow cell system with three poly(methyl methacrylate) (PMMA) plates to divide the anolyte, catholyte and CO_2 gas chambers, respectively. The anion exchange membrane (Fumasep FAB-PK-130, Fuel Cell Store) was placed between the anolyte and catholyte chambers for separation of the electrolyte and the exchange of anions. Nickel foam of size 3 × 3 cm^2 was used as the anode, counter electrode. The Ag/AgCl (3.5 M KCl) reference electrode was put in the cathode compartment. A total of 11.5 mg VS-Bi_2O_3 was mixed with 25 μL Sustainion™ XA-9 solution and 1 mL dispersion liquid (isopropanol : H_2O = 3 : 1, v/v), followed by ultrasonication for 30 min to form an ink, which was then sprayed onto a piece of commercial Sigracet gas diffusion layer (GDS 28BC, Fuel Cell store), whose area was set as 3 × 3 cm^2. After drying, a piece of 1.5 × 1.5 cm^2 gas diffusion electrode (GDE) was tested using a flow cell reactor as the working electrode. The CO_2 gas feed rate was set as 20 standard cubic centimeters per minute (sccm). The electrolyte was 1 M KOH, which flows at a rate of 10 mL per min. All potentials were calibrated to the reversible hydrogen electrode (RHE) with iR_{cell} compensation (i serves as the applied current and R_{cell} denotes the cell resistance) according to the equation $E_{RHE} = E_{Ag/AgCl} + 0.205 + 0.059 \times pH + i \times R_{cell}$. Gas products were analyzed *via* gas chromatography (RAMIN, GC2060), using a thermal conductivity detector (TCD) for detecting H_2 and a flame ionization detector (FID) for the detection of CO and other gaseous hydrocarbons. The liquid product of $HCOO^-$ was quantified using ^{1}H nuclear magnetic resonance (NMR). For analysis, 500 μL electrolyte with the liquid product in it was taken out to mix with 100 μL D_2O (with TMSP as the internal standard) to form the mixture quantified later using NMR.

Results and discussion

XRD measurements were performed in order to figure out the phase of the product. In Fig. 1a, the XRD pattern of the obtained VS-Bi_2O_3 matches with cubic Bi_2O_3 (PDF#27-0052), revealing its cubic phase. Besides, the wide peaks indicate its weak crystallinity with peaks at 27.9°, 46.4° and 55.1° corresponding to the (111), (220) and (311) facets, respectively.

The scanning electron microscopy (SEM) images (Fig. 1b and c, and Fig. S1 and S2, ESI†) show a vegetable sponge-like morphology, assembling multiple pieces of nanosheets into a hierarchical micron structure. Transmission electron microscopy (TEM) results (Fig. 1d and e and Fig. S3, ESI†) show lots of open pores in the VS-Bi_2O_3. Moreover, the high-resolution TEM (HR-TEM; Fig. 1f) image displays no obvious lattice fringe. The selected area electron diffraction (SAED; inset in Fig. 1f) image exhibits a diffraction ring with a radius of 3.19 Å that corresponds to the (111) plane of Bi_2O_3 (PDF#27-0052), confirming the weak crystallinity of VS-Bi_2O_3. The B-Bi_2O_3 obtained from the VS-Bi_2O_3 *via* annealing in air has a high crystallinity, with the XRD pattern aligning well with monoclinic Bi_2O_3 (PDF#41-1449) (Fig. S4, ESI†).

The CO_2RR processes for VS-Bi_2O_3 and B-Bi_2O_3 were carried out in 1 M KOH electrolyte (pH = 14) using a flow cell system (Fig. S5, ESI†). During the CO_2RR, VS-Bi_2O_3 underwent *in situ* reconstruction according to the XRD measurements for different electrolysis times. As shown in Fig. 2a, tetragonal $Bi_2O_2CO_3$ (PDF#41-1488) appeared after 0.5 h of electrolysis at 100 mA cm^{-2}. As the catalysis process proceeds, the featured peaks of $Bi_2O_2CO_3$ (marked with purple stars) become noticeable for the XRD patterns after 3, 10, and 20 h. Furthermore, the Raman spectrum of the VS-Bi_2O_3 sample after electrolysis also demonstrates the formed $Bi_2O_2CO_3$ *via* the featured peaks appearing at 162 and 1069 cm^{-1} (in light orange shadow),[22,34] while the peak at 95 cm^{-1} is attributed to Bi_2O_3 (in light grey shadow) (Fig. 2b).[35] As for B-Bi_2O_3, scarce $Bi_2O_2CO_3$ was detected after electrolysis (Fig. S6, ESI†).

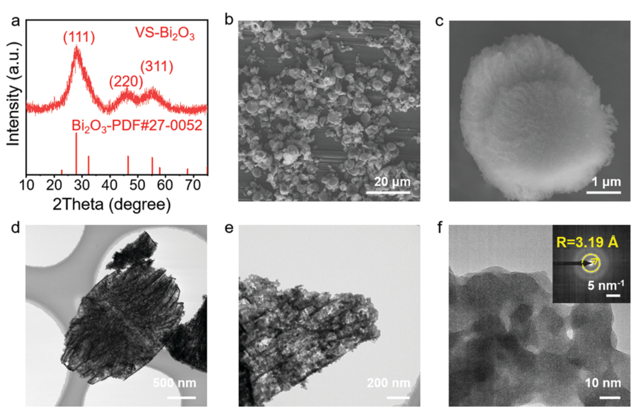

Fig. 1 (a) XRD pattern of VS-Bi_2O_3 in which the wide peaks indicate the weak crystallinity of VS-Bi_2O_3. (b and c) SEM images of VS-Bi_2O_3 showing the vegetable sponge-like morphology. (d and e) TEM images of VS-Bi_2O_3 showing lots of open pores. (f) HR-TEM image of VS-Bi_2O_3 displaying no obvious lattice fringe, and (inset) SAED image exhibiting a classic diffraction ring of Bi_2O_3 (PDF#27-0052).

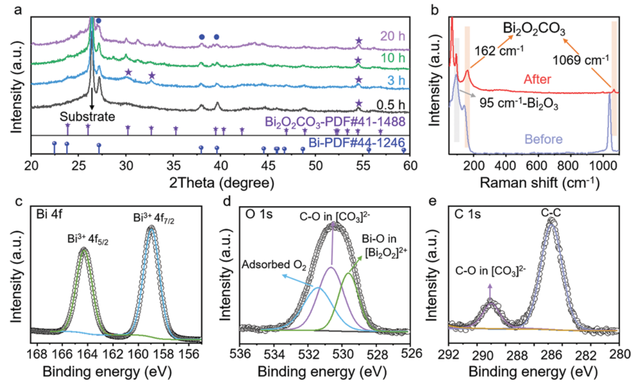

Fig. 2 (a) XRD patterns of VS-Bi_2O_3 electrolyzing the CO_2RR at 100 mA cm^{-2} after 0.5, 3, 10 and 20 h, respectively. $Bi_2O_2CO_3$ and Bi were formed and maintained during the CO_2RR. (b) Raman spectra of VS-Bi_2O_3 before (blue line) and after (red line) the CO_2RR for 3 h. $Bi_2O_2CO_3$ (orange shadow) is formed in the electrolytic process. (c–e) Bi 4f, O 1s and C 1s XPS spectra, respectively, of the post-electrolysis VS-Bi_2O_3 (at 100 mA cm^{-2} for 24 h), demonstrating the existence of $Bi_2O_2CO_3$.

To further analyse the surface valence states, X-ray photoelectron spectroscopy (XPS) was conducted. Post-electrolysis XPS inspections of VS-Bi_2O_3 (at 100 mA cm^{-2} for 24 h) are shown in Fig. 2c–e. The peaks at 159 and 164.3 eV in the Bi 4f spectrum (Fig. 2c) are assigned to Bi^{3+}, demonstrating a single oxidation state of Bi^{3+}.[28,30] Three obvious fitted peaks can be clearly identified in the O 1s spectrum (Fig. 2d). The peaks at 529.6, 530.7 and 531.5 eV correspond to the O atoms in the Bi–O bonds in the $[Bi_2O_2]^{2+}$ layers, the O atoms in C–O in the $[CO_3]^{2-}$ layers, and the oxygen of adsorbed O_2, respectively.[7,28,34] As for the C 1s XPS spectrum (Fig. 2e), the peak at 289.0 eV is indexed to the carbon atoms in the $[CO_3]^{2-}$ layers.[36] XPS spectroscopy verifies the existence of $Bi_2O_2CO_3$ after electroreduction, in line with the XRD and Raman results.

To gain further insight into the morphology changes, SEM, TEM and HR-TEM characterizations of the post-electrolysis sample of VS-Bi_2O_3 were carried out. As shown in Fig. 3a and b, vegetable sponge-like frames of VS-Bi_2O_3 evolve into a nanosheet morphology after CO_2RR for 10 h. Combined with more post-electrolysis SEM images for different timescales in Fig. S7 and S8 (ESI†), we speculate that the morphology of VS-Bi_2O_3 underwent several transformation steps under different cathodic potentials. The shape first transformed from the vegetable sponge-like to thick nanosheet-assembled plates, and

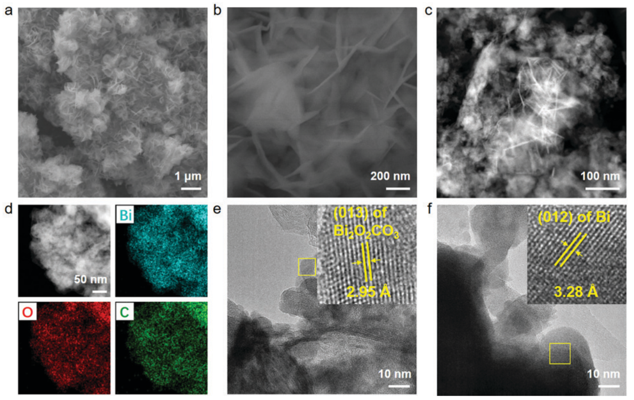

Fig. 3 (a and b) SEM, (c) TEM and (d) STEM-EDS elemental maps of VS-Bi_2O_3 after the CO_2RR for 10 h. (e and f) HR-TEM images of VS-Bi_2O_3 after the CO_2RR for 10 h in which $Bi_2O_2CO_3$ and metallic Bi are detected *via* their characteristic facets.

then gradually changed into thin nanosheets. The TEM image (Fig. 3c) confirms the nanosheet morphology in accordance with the SEM images. The SEM images after electrolysis of B-Bi_2O_3 are also displayed in Fig. S9 and S10 (ESI†). Scanning transmission electron microscopy-energy dispersive spectroscopy (STEM-EDS; Fig. 3d) shows the uniformly distributed Bi, O and C elements. It is worth noting that the presence of the carbon element to some extent reveals the existence of $Bi_2O_2CO_3$. The high-resolution TEM image in Fig. 3e proves this point as well, with the lattice spacing of 2.95 Å aligning well with the (013) facet of $Bi_2O_2CO_3$. Fig. 3f shows a 3.28 Å lattice space in accordance with the (012) plane of metallic bismuth, which was derived from the *in situ* reduction of VS-Bi_2O_3.

The above measurements illustrate that the prepared VS-Bi_2O_3 is prone to undergo reconstruction under the working conditions. The sample was changed into metallic bismuth and $Bi_2O_2CO_3$ after electrolysis, among which the $Bi_2O_2CO_3$ did not appear in the B-Bi_2O_3 sample (Fig. S6, ESI†). Besides, the porous vegetable sponge-like morphology is inclined to be exposed to the operating environment since its open pores can be filled with electrolytes and reactants. This may lead to the reconstruction from VS-Bi_2O_3 to Bi and $Bi_2O_2CO_3$ during the CO_2RR process. $Bi_2O_2CO_3$ is a layered structure consisting of CO_3^{2-} and $[Bi_2O_2]^{2+}$, which has been reported to exhibit a lower overpotential compared with metallic bismuth.[37]

To figure out the phase transformation from Bi_2O_3 to $Bi_2O_2CO_3$ and Bi, three XRD samples obtained under different conditions were prepared (Table S1 and Fig. S11, ESI†). The results indicate that VS-Bi_2O_3 did not react directly with the KOH electrolyte in the absence of CO_2 under ambient conditions. However, when VS-Bi_2O_3 was introduced into the CO_2 atmosphere, $Bi_2O_2CO_3$ was generated with no metallic Bi formed. Furthermore, the VS-Bi_2O_3 changed into metallic Bi and $Bi_2O_2CO_3$ with the current density applied. Based on the above results, we speculated that the $Bi_2O_2CO_3$ might be formed *via* the intercalation of CO_3^{2-} into the layered structure of the bismuth oxide compound. Previous reports have revealed that the presence of CO_2 during the CO_2RR process plays a significant role in maintaining the stable existence of $Bi_2O_2CO_3$ thanks to the consumption of most cathodic electrons.[37,38] Besides, a high local pH was also reported to be beneficial for the formation of $Bi_2O_2CO_3$, and the 1 M KOH electrolyte in this work can provide a large amount of OH^-, which might promote the generation of $Bi_2O_2CO_3$.[7]

We then carried out the CO_2RR to assess the electrocatalytic performance and identify the role of $Bi_2O_2CO_3$. As shown in Fig. 4a and Fig. S12 (ESI†), VS-Bi_2O_3 achieves a high current density of up to 100 mA cm^{-2} at a small applied potential of only −0.53 V, with an accompanying high FE($HCOO^-$) of around 93.6%. The FE($HCOO^-$) remains at a high level of >93.0% over a wide potential range from −0.53 V to −1.29 V, with a potential window of 760 mV. The maximum FE($HCOO^-$) of 94.9% appears at −1.12 V delivering a current density of 300 mA cm^{-2}. The overall current density of 400 mA cm^{-2} is achieved at a potential of −1.29 V, in the meantime sustaining a high FE($HCOO^-$) of around 93.7%. As for the contrast sample, B-Bi_2O_3 attains the same current density with a much more negative potential and a much lower selectivity for formate. Taking the current density of 200 mA cm^{-2}, for example, B-Bi_2O_3 needs an applied potential of −1.11 V to reach that goal, which is 380 mV more negative than VS-Bi_2O_3 with a low FE($HCOO^-$) of 85.3% under the operational conditions (Fig. 4b, and Fig. S13, ESI†). Furthermore, the potential grows markedly for the larger current densities, and a potential of −1.58 V is needed for 400 mA cm^{-2}, negatively shifted by 300 mV compared with VS-Bi_2O_3. The CO_2RR performance measurements unveil the superb activity and exclusive selectivity of VS-Bi_2O_3 for the electrochemical conversion of CO_2 into formate, indicating the significance of $Bi_2O_2CO_3$ derived from VS-Bi_2O_3.

Since efficient charge transfer at the catalyst/electrolyte interface is beneficial to the catalytic process, we carried out electrochemical impedance spectroscopy (EIS) in order to measure the kinetics of charge transfer.[35] Fig. 4c shows the Nyquist plots of VS-Bi_2O_3 and B-Bi_2O_3 under open-circuit potential at a steady state, from which a smaller arc can be observed in VS-Bi_2O_3 (red) compared with B-Bi_2O_3 (blue). In the Nyquist plots, the charge transfer resistance (R_{ct}) of the electrochemical reaction can be represented by the radius of the arc, and a smaller arc usually means a smaller resistance. Thus, VS-Bi_2O_3 possesses a highly accelerated charge-transfer process thanks to its much shorter radius than the contrast bulk sample. We attributed this remarkable improvement to the appearance of $Bi_2O_2CO_3$ derived from VS-Bi_2O_3. Hence durability testing was carried out at the current density of 100 mA cm^{-2}, and the potential remained steady without any significant degradation for an electrolysis process of over 18 h, demonstrating its superior stability for converting CO_2 to formate (Fig. 4d). The performance comparison of VS-Bi_2O_3 with previous Bi-based materials is listed in Table S2 (ESI†).

$Bi_2O_2CO_3$ is a layered structure consisting of CO_3^{2-} and $[Bi_2O_2]^{2+}$.[37] The presence of metastable oxides has previously been reported to be able to stabilize the reduced CO_2 intermediate, which plays a vital role in lowering the overpotential

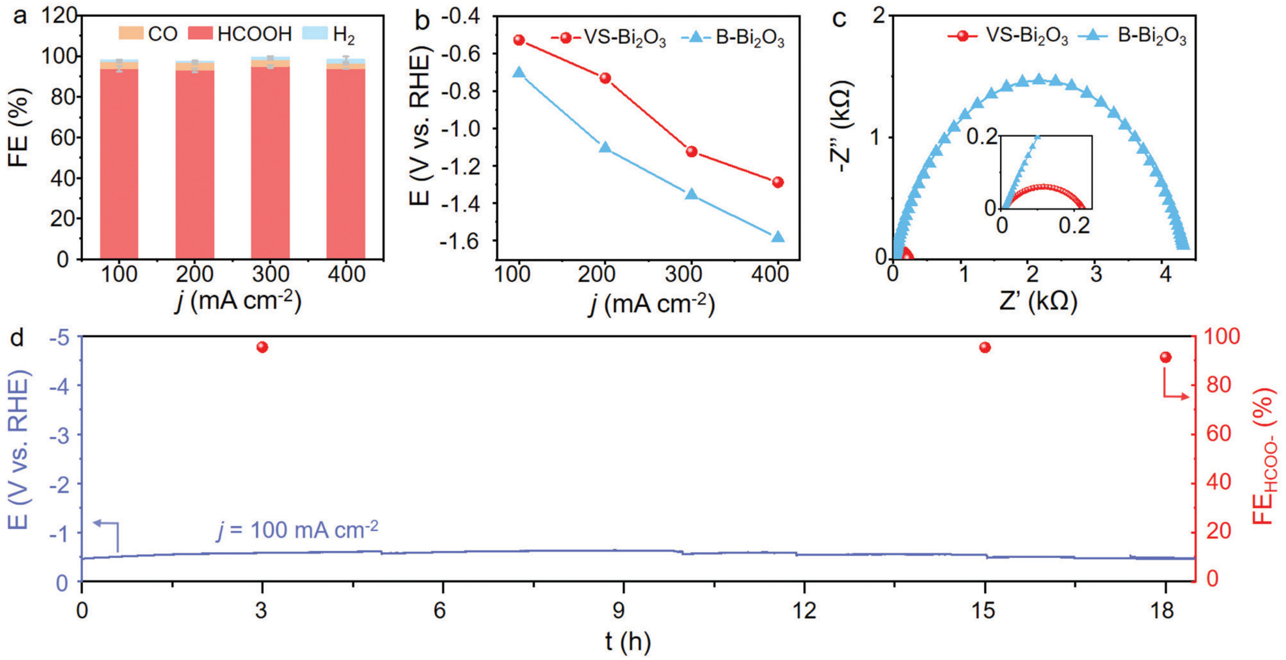

Fig. 4 (a) Faradaic efficiencies plot (with error bars) of VS-Bi_2O_3 in 1 M KOH electrolyte using a flow cell system. (b) Current density dependence of potential values for VS-Bi_2O_3 and B-Bi_2O_3. (c) Fitting results of Nyquist plots for VS-Bi_2O_3 and B-Bi_2O_3 under open-circuit potential at a steady state, where the inset shows an expanded version of the area near the origin. (d) Stability testing of VS-Bi_2O_3 at 100 mA cm^{-2}.

and accelerating the charge transfer required to reduce CO_2 into the target formate product.[7,37–39] The $Bi_2O_2CO_3$ was generated *in situ* from VS-Bi_2O_3 during the CO_2RR process, whose existence after electrolysis at 100 mA cm^{-2} for 20 h revealed that the formed $Bi_2O_2CO_3$ was robust enough to survive under an applied cathodic bias. However, the contrast sample B-Bi_2O_3 was reduced *in situ* to metallic Bi without $Bi_2O_2CO_3$ and was accompanied by an unsatisfactory performance. Therefore, the presence of $Bi_2O_2CO_3$ might play a significant role in enhancement of the CO_2RR performance.

Conclusions

In summary, through the adoption of a facile microwave/ultrasonic synthesis method, we fabricated the porous vegetable sponge-like bismuth oxide (VS-Bi_2O_3), which underwent *in situ* reconstruction to form metallic Bi and $Bi_2O_2CO_3$ nanosheets, exhibiting excellent CO_2RR activity with near-unity formate selectivity under a high current density of 400 mA cm^{-2}. Besides, the durability at 100 mA cm^{-2} could reach over 18 h, suggesting its remarkable long-term stability. A series of characterization measurements, such as post-electrolysis XRD, Raman, and TEM, indicate the existence of $Bi_2O_2CO_3$, revealing its robust stability. We further demonstrate that the porous vegetable sponge-like configuration may play a critical role in the *in situ* reconstruction to form $Bi_2O_2CO_3$, and that the appearance of $Bi_2O_2CO_3$ could enhance the CO_2RR performance. This study emphasizes the significance of the precatalyst structure on its *in situ* reconstruction and CO_2RR performance optimization.

Author contributions

Hua Gui Yang, Fangxin Mao and Peng Fei Liu designed and guided the study; Yingli Shi and Chun Fang Wen performed the experiments and analyzed the experimental data; Xuefeng Wu carried out the TEM experiments; Jia Yue Zhao helped in the analysis. All the authors discussed and commented on the data and contributed to the manuscript.

Conflicts of interest

There are no conflicts to declare.

Acknowledgements

This work was financially supported by the National Natural Science Funds for Distinguished Young Scholars (51725201), the International (Regional) Cooperation and Exchange Projects of the National Natural Science Foundation of China (51920105003), the Innovation Program of Shanghai Municipal Education Commission (E00014), the Science and Technology Commission of Shanghai Municipality (21DZ1207101), the National Natural Science Foundation of China (51902105, 52103340), the Fundamental Research Funds for the Central Universities (JKD01211519), the China Postdoctoral Science Foundation Funded Project (2020M681201), and the Shanghai Engineering Research Center of Hierarchical Nanomaterials (18DZ2252400). The authors also thank the Frontiers Science Center for Materiobiology and Dynamic Chemistry.

Notes and references

1 G. Wang, J. Chen, Y. Ding, P. Cai, L. Yi, Y. Li, C. Tu, Y. Hou, Z. Wen and L. Dai, Electrocatalysis for CO_2 conversion: from fundamentals to value-added products, *Chem. Soc. Rev.*, 2021, **50**, 4993–5061.

2 J. Jeong, J. S. Kang, H. Shin, S. H. Lee, J. Jang, T. Hyeon, H. S. Park and Y. E. Sung, Self-supported mesoscopic tin oxide nanofilms for electrocatalytic reduction of carbon dioxide to formate, *Chem. Commun.*, 2021, **57**, 3445–3448.

3 X. Tan, C. Yu, Y. Ren, S. Cui, W. Li and J. Qiu, Recent advances in innovative strategies for the CO_2 electroreduction reaction, *Energy Environ. Sci.*, 2021, **14**, 765–780.

4 S. Zhang, Q. Fan, R. Xia and T. J. Meyer, CO_2 reduction: from homogeneous to heterogeneous electrocatalysis, *Acc. Chem. Res.*, 2020, **53**, 255–264.

5 D. H. Nam, P. De Luna, A. Rosas-Hernandez, A. Thevenon, F. Li, T. Agapie, J. C. Peters, O. Shekhah, M. Eddaoudi and E. H. Sargent, Molecular enhancement of heterogeneous CO_2 reduction, *Nat. Mater.*, 2020, **19**, 266–276.

6 T. Zheng, C. Liu, C. Guo, M. Zhang, X. Li, Q. Jiang, W. Xue, H. Li, A. Li, C. W. Pao, J. Xiao, C. Xia and J. Zeng, Copper-catalysed exclusive CO_2 to pure formic acid conversion via single-atom alloying, *Nat. Nanotechnol.*, 2021, **16**, 1386–1393.

7 T. Fan, W. Ma, M. Xie, H. Liu, J. Zhang, S. Yang, P. Huang, Y. Dong, Z. Chen and X. Yi, Achieving high current density for electrocatalytic reduction of CO_2 to formate on bismuth-based catalysts, *Cell Rep. Phys. Sci.*, 2021, **2**, 100353.

8 R. I. Masel, Z. Liu, H. Yang, J. J. Kaczur, D. Carrillo, S. Ren, D. Salvatore and C. P. Berlinguette, An industrial perspective on catalysts for low-temperature CO_2 electrolysis, *Nat. Nanotechnol.*, 2021, **16**, 118–128.

9 L. Yi, J. Chen, P. Shao, J. Huang, X. Peng, J. Li, G. Wang, C. Zhang and Z. Wen, Molten-salt-assisted synthesis of bismuth nanosheets for long-term continuous electrocatalytic conversion of CO_2 to formate, *Angew. Chem., Int. Ed.*, 2020, **59**, 20112–20119.

10 K. Ye, Z. Zhou, J. Shao, L. Lin, D. Gao, N. Ta, R. Si, G. Wang and X. Bao, *In situ* reconstruction of a hierarchical Sn-Cu/SnO_x core/shell catalyst for high-performance CO_2 electroreduction, *Angew. Chem., Int. Ed.*, 2020, **59**, 4814–4821.

11 W. Zhang, S. Yang, M. Jiang, Y. Hu, C. Hu, X. Zhang and Z. Jin, Nanocapillarity and nanoconfinement effects of pipet-like bismuth@carbon nanotubes for highly efficient electrocatalytic CO_2 reduction, *Nano Lett.*, 2021, **21**, 2650–2657.

12 L. Sun, V. Reddu, A. C. Fisher and X. Wang, Electrocatalytic reduction of carbon dioxide: opportunities with heterogeneous molecular catalysts, *Energy Environ. Sci.*, 2020, **13**, 374–403.

13 X. Fu, A. Zhu, X. Chen, S. Zhang, M. Wang and M. Yuan, Stabilization of Cu/Ni alloy nanoparticles with graphdiyne enabling efficient CO_2 reduction, *Chem. Res. Chin. Univ.*, 2021, **37**, 1328–1333.

14 Q. Gong, P. Ding, M. Xu, X. Zhu, M. Wang, J. Deng, Q. Ma, N. Han, Y. Zhu, J. Lu, Z. Feng, Y. Li, W. Zhou and Y. Li, Structural defects on converted bismuth oxide nanotubes enable highly active electrocatalysis of carbon dioxide reduction, *Nat. Commun.*, 2019, **10**, 2807.

15 N. Han, P. Ding, L. He, Y. Li and Y. Li, Promises of main group metal-based nanostructured materials for electrochemical CO_2 reduction to formate, *Adv. Energy Mater.*, 2019, **10**, 1902338.

16 N. Han, Y. Wang, H. Yang, J. Deng, J. Wu, Y. Li and Y. Li, Ultrathin bismuth nanosheets from *in situ* topotactic transformation for selective electrocatalytic CO_2 reduction to formate, *Nat. Commun.*, 2018, **9**, 1320.

17 F. Yang, A. O. Elnabawy, R. Schimmenti, P. Song, J. Wang, Z. Peng, S. Yao, R. Deng, S. Song, Y. Lin, M. Mavrikakis and W. Xu, Bismuthene for highly efficient carbon dioxide electroreduction reaction, *Nat. Commun.*, 2020, **11**, 1088.

18 Z. Wu, H. Wu, W. Cai, Z. Wen, B. Jia, L. Wang, W. Jin and T. Ma, Engineering bismuth-tin interface in bimetallic aerogel with a 3D porous structure for highly selective electrocatalytic CO_2 reduction to HCOOH, *Angew. Chem., Int. Ed.*, 2021, **60**, 12554–12559.

19 M. Zhang, W. Wei, S. Zhou, D.-D. Ma, A. Cao, X.-T. Wu and Q.-L. Zhu, Engineering a conductive network of atomically thin bismuthene with rich defects enables CO_2 reduction to formate with industry-compatible current densities and stability, *Energy Environ. Sci.*, 2021, **14**, 4998–5008.

20 J. Yang, X. Wang, Y. Qu, X. Wang, H. Huo, Q. Fan, J. Wang, L. M. Yang and Y. Wu, Bi-based metal-organic framework derived leafy bismuth nanosheets for carbon dioxide electroreduction, *Adv. Energy Mater.*, 2020, **10**, 2001709.

21 Y. Zhou, R. Zhou, X. Zhu, N. Han, B. Song, T. Liu, G. Hu, Y. Li, J. Lu and Y. Li, Mesoporous PdAg nanospheres for stable electrochemical CO_2 reduction to formate, *Adv. Mater.*, 2020, **32**, 2000992.

22 D. Yao, C. Tang, A. Vasileff, X. Zhi, Y. Jiao and S. Z. Qiao, The controllable reconstruction of Bi-MOFs for electrochemical CO_2 reduction through electrolyte and potential mediation, *Angew. Chem., Int. Ed.*, 2021, **60**, 18178–18184.

23 F. Pan and Y. Yang, Designing CO_2 reduction electrode materials by morphology and interface engineering, *Energy Environ. Sci.*, 2020, **13**, 2275–2309.

24 P. F. Liu, M. Y. Zu, L. R. Zheng and H. G. Yang, Bismuth oxyiodide microflower-derived catalysts for efficient CO_2 electroreduction in a wide negative potential region, *Chem. Commun.*, 2019, **55**, 12392–12395.

25 J. Fan, X. Zhao, X. Mao, J. Xu, N. Han, H. Yang, B. Pan, Y. Li, L. Wang and Y. Li, Large-area vertically aligned bismuthene nanosheet arrays from galvanic replacement reaction for efficient electrochemical CO_2 conversion, *Adv. Mater.*, 2021, **33**, 2100910.

26 H. Jiang, Q. He, Y. Zhang and L. Song, Structural self-reconstruction of catalysts in electrocatalysis, *Acc. Chem. Res.*, 2018, **51**, 2968–2977.

27 W. Ma, J. Bu, Z. Liu, C. Yan, Y. Yao, N. Chang, H. Zhang, T. Wang and J. Zhang, Monoclinic scheelite bismuth vanadate derived bismuthene nanosheets with rapid kinetics for electrochemically reducing carbon dioxide to formate, *Adv. Funct. Mater.*, 2020, **31**, 2006704.

28 P. Deng, H. Wang, R. Qi, J. Zhu, S. Chen, F. Yang, L. Zhou, K. Qi, H. Liu and B. Y. Xia, Bismuth oxides with enhanced bismuth-oxygen structure for efficient electrochemical reduction of carbon dioxide to formate, *ACS Catal.*, 2020, **10**, 743–750.
29 C. Yang, J. X. Chai, Z. Wang, Y. L. Xing, J. Peng and Q. Y. Yan, Recent progress on bismuth-based nanomaterials for electrocatalytic carbon dioxide reduction, *Chem. Res. Chin. Univ.*, 2020, **36**, 410–419.
30 Z. Chen, K. Mou, X. Wang and L. Liu, Nitrogen-doped graphene quantum dots enhance the activity of Bi_2O_3 nanosheets for electrochemical reduction of CO_2 in a wide negative potential region, *Angew. Chem., Int. Ed.*, 2018, **57**, 12790–12794.
31 T. Tran-Phu, R. Daiyan, Z. Fusco, Z. Ma, R. Amal and A. Tricoli, Nanostructured β-Bi_2O_3 fractals on carbon fibers for highly selective CO_2 electroreduction to formate, *Adv. Funct. Mater.*, 2020, **30**, 1906478.
32 S. Liu, X. F. Lu, J. Xiao, X. Wang and X. W. Lou, Bi_2O_3 nanosheets grown on multi-channel carbon matrix to catalyze efficient CO_2 electroreduction to HCOOH, *Angew. Chem., Int. Ed.*, 2019, **58**, 13828–13833.
33 M.-G. Ma, J.-F. Zhu, R.-C. Sun and Y.-J. Zhu, Microwave-assisted synthesis of hierarchical Bi_2O_3 spheres assembled from nanosheets with pore structure, *Mater. Lett.*, 2010, **64**, 1524–1527.
34 A. Dutta, I. Zelocualtecatl Montiel, K. Kiran, A. Rieder, V. Grozovski, L. Gut and P. Broekmann, A tandem ($Bi_2O_3 \rightarrow Bi_{met}$) catalyst for highly efficient ec-CO_2 conversion into formate: operando Raman spectroscopic evidence for a reaction pathway change, *ACS Catal.*, 2021, **11**, 4988–5003.
35 P. Deng, F. Yang, Z. Wang, S. Chen, Y. Zhou, S. Zaman and B. Y. Xia, Metal-organic framework-derived carbon nanorods encapsulating bismuth oxides for rapid and selective CO_2 electroreduction to formate, *Angew. Chem., Int. Ed.*, 2020, **59**, 10807–10813.
36 M. Favaro, H. Xiao, T. Cheng, W. A. Goddard III, J. Yano and E. J. Crumlin, Subsurface oxide plays a critical role in CO_2 activation by Cu(111) surfaces to form chemisorbed CO_2, the first step in reduction of CO_2, *Proc. Natl. Acad. Sci. U. S. A.*, 2017, **114**, 6706–6711.
37 Y. Zhang, X. Zhang, Y. Ling, F. Li, A. M. Bond and J. Zhang, Controllable synthesis of few-layer bismuth subcarbonate by electrochemical exfoliation for enhanced CO_2 reduction performance, *Angew. Chem., Int. Ed.*, 2018, **130**, 13467–13471.
38 Y. Shi, Y. Ji, J. Long, Y. Liang, Y. Liu, Y. Yu, J. Xiao and B. Zhang, Unveiling hydrocerussite as an electrochemically stable active phase for efficient carbon dioxide electroreduction to formate, *Nat. Commun.*, 2020, **11**, 3415.
39 Z. Tao and H. Wang, $Pb_3(CO_3)_2(OH)_2$ is an active phase in electrocatalytic CO_2 reduction to formate, *Chem. Res. Chin. Univ.*, 2020, **36**, 1145–1146.